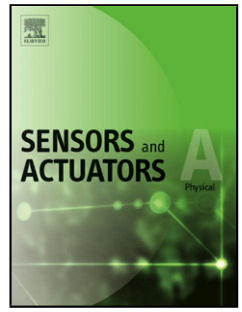

Title: Dynamical switching of an electromagnetically driven compliant bistable mechanism

Authors: Dung-An Wang, Huy-Tuan Pham, Yi-Han Hsieh

PII: S0924-4247(08)00535-9
DOI: doi:10.1016/j.sna.2008.11.004
Reference: SNA 6440

To appear in: *Sensors and Actuators A*

Received date: 20-7-2008
Revised date: 16-9-2008
Accepted date: 2-11-2008

Dynamical switching of an electromagnetically driven compliant bistable mechanism

Dung-An Wang, Huy-Tuan Pham and Yi-Han Hsieh

Institute of Precision Engineering, National Chung Hsing University, Taichung 515, Taiwan, ROC

E-mail: daw@dragon.nchu.edu.tw

Abstract

Dynamical switching behaviors of a compliant bistable mechanism driven by electromagnetic force are investigated. The bistability of the mechanism originates from combined tension and bending of the beam structures. Finite element analyses are used to characterize the bistability of the mechanism under static loading. An analytical model is developed to analyze the dynamic behaviors of the mechanism. The main advantage of this dynamic actuation method is the absence of on-chip driving mechanisms. The dynamical switching characteristics of the bistable mechanism are examined. Microscale prototypes are fabricated and tested. Using the driving technique, we demonstrate dynamical switching in the fabricated device and verify that the performance predicted by theory is attained.

Keywords: Bistable; Electromagnetic; Switching

* Corresponding author: Tel.:+886-4-22840531 ext. 365; fax:+886-4-22858362

E-mail address: daw@nchu.edu.tw (D.-A. Wang).

1. Introduction

Bistable micromechanisms (BMs) are gaining attention in MEMS applications such as accelerometers [1], memory cells [2], switches [3-6], relays [7-9], valves [10] and feeding systems [11]. One advantage of BMs is that no power is required to keep the mechanism in either of its bistable positions [12,13]. Low actuation force and power, high cycle life, and predictable, repeatable motion are required for a BM in MEMS applications [12].

Various actuation methods of BMs have been proposed including electrothermal actuation [9,12,14], electrostatic actuation [6,15-19], electromagnetic actuation [20,21], optical actuation [22] and piezoelectric actuation [23]. Depending on different application requirements, an appropriate actuation method should be selected. Built-in driving mechanisms are usually required for electrothermal and electrostatic actuations as reported previously [9,12,14-19]. Sulfridge et al. [22] reported an optical switch for a MEMS bistable beam using a laser light. The laser being used is 200 mW and a load of 0.6 nN is generated. It might not be convenient for MEMS devices requiring actuation forces on the μN scale. The meso-scale piezoelectric bistable beam described by Giannopoulos et al. [23] needs a high driving voltage up to 120 V and a precompression of the beam is needed for snap-through action.

Cao et al. [21] demonstrated a bi-directional MEMS actuator based on electrothermal buckling and electromagnetic Lorenz force. These type of actuators require relatively low voltages and high currents to operate and can exert large forces on the mN scale. Electromagnetic actuation can be used in MEMS applications that require high displacement, high force and bi-directional actuation. An external vibration can be utilized to move a BM between its bistable positions based on an investigation carried out by Kreider and Nayfeh [24] for a buckled beam under harmonic excitation. A harmonic or intermittent snap-through behavior of their prebuckled beam is observed. The harmonic excitation by electromagnetic forcing provides a way for motion control of BMs that require high displacement output and high force actuation.

This paper describes a design of a vibration-actuated BM. The vibration exploited to switch the on-substrate BM is provided by an electromagnetic Lorenz force, requiring no need for built-in driving mechanisms such as electrothermal or electrostatic actuators. The electromagnetic actuation is based on the actuation method reported by Cao et al. [21] and Ko et al. [20], where a precompressed beam is moving through the full range of its bi-directional motion [21] or a bistable beam is actuated statically [20]. Dissimilar to their design, the BM are switched dynamically by shaking the device with an alternating electromagnetic force. An analytical model of the BM is derived in order to analyze its dynamic behavior. Prototypes of the device are fabricated using an electroforming process. Experiments are carried out to demonstrate the effectiveness of the dynamical switching of the BM.

2. Design

2.1 Operational principle

A schematic of a BM and a permanent magnet served to actuate the mechanism is shown in Fig. 1(a). A Cartesian coordinate system is also shown in the figure. The mechanism is a compliant chevron-type mechanism consisting of a shuttle mass, flexible hinges, hinged beams and lateral springs. The flexible hinges facilitate the rotation of the hinged beams. Upon the application of an actuation force F to the hinged beams, the flexible hinges and lateral springs deflect, releasing the strain energy while the mechanism moves towards the other stable equilibrium state. Fig. 2 shows the two stable equilibrium states of the mechanism.

An electromagnetic effect is utilized to perform the bi-directional, in-plane motions. As shown in Fig. 1(a), the mechanism is placed in a magnetic field B. As a current I passes through the contact pads, each beam experiences a force perpendicular to both the directions of the current and magnetic field. The force exerted on each beam can be expressed as

$$F_m = \frac{I}{2} l \times B \tag{1}$$

We represent the section of the beam by a vector l along the beam and in the direction of the current as shown in Fig. 1(b). If the B field is perpendicular to the substrate and the beam makes an angle θ with the y axis, see Fig. 1(b), the resultant force F exerted to the mechanism is given by

$$F = 4F_m \cos\theta \tag{2}$$

When the current direction is switched, the direction of F is reversed and the bi-directional motion of the mechanism can be controlled.

Fig. 3 illustrates a four-step operation of the mechanism. First, an AC current I_1 of frequency ω_1 is passed though the hinged beams through the two contact pads. The vibration induced by the electromagnetic actuation resonates the mechanism (see Fig. 3(a)), causing it to move towards its second stable position (SSP) (see Fig. 3(b)). Next, an AC current I_2 of frequency ω_2 is applied. This induced vibration resonates the mechanism (see Fig. 3(c)), causing it to move towards its first stable position (FSP) (see Fig. 3(d)). This dynamical switching of the BM via an external magnetic field and an applied AC current provides with a simple means of controlling motion of the mechanism in the absence of on-chip driving mechanisms.

When exciting the mechanism dynamically, the actual vibration of the mechanism is always a combination or mixture of all the vibration modes. If the in-plane mode is favored, out-of-plane modes of vibration cause the mechanism to deform perpendicular to the substrate which is not desired for efficient operation of the BM. Therefore, the mechanism should have high stiffness in the out-of-plane direction and the exciting frequency should be carefully selected to avoid undesired vibration modes.

2.2 Modeling

An equation of motion of a lumped parameter model of the BM shown in Fig. 1(a) is derived to analyze its dynamic behavior. Fig. 4 shows a schematic of the mechanism and a Cartesian coordinate system. It is assumed that the out-of-plane motion of the mechanism is small and does not affect its in-plane motion. The equation of motion for a simple mass-damper-spring system with excitation F from electromagnetic actuation has the form

$$m\ddot{x} + c\dot{x} + kx = F \tag{3}$$

where m, c, and k are the mass, damping coefficient, and spring stiffness of the mechanism, respectively. Assuming Stoke's damping between the substrate and the mechanism, c can be expressed as [25,26]

$$c = \mu A \beta \left(1 + \frac{\sinh 2\beta d + \sin 2\beta d}{\cosh 2\beta d - \cos 2\beta d} \right) \tag{4}$$

$$\beta = \sqrt{\frac{\omega}{2\nu}} \tag{5}$$

where μ and ν are the dynamic and kinematic viscosity of the fluid in the environment, respectively. A and d are the planar area of the mechanism and the gap between the substrate and the mechanism, respectively. ω is the frequency of the AC current passing through the mechanism. When the mechanism is actuated by an AC current $I = i\sin(\omega t)$, using Eqs. (1) and (2), the electromagnetic force F exerted to the mechanism is

$$F = 2ilB\cos\theta\sin(\omega t) \tag{6}$$

where i and ω are the amplitude and frequency of the applied AC current, respectively.

The nonlinear spring stiffness k can be taken as the slope of the tangent to the force-displacement (f-d) curve of the mechanism. For a compliant chevron-type BM shown in Fig. 4, a typical f-d curve is depicted in Fig. 5. The f-d curve has three characteristic regions of stiffness. There are two short regions of positive stiffness at the beginning and the end of the curve, and a long region of negative stiffness in between. In order to model the highly nonlinear spring stiffness for this type of mechanism, Qiu et al. [27] used a mode superposition method, where the first three buckling modes for a straight beam were used as the superposition basis for deflection shape of an initially curved beam. Applying the theory of the pseudo-rigid-body model [28], Casals-Terre and Shkel [17] obtained a f-d relation for a compliant BM. In order to accurately predict the f-d relation by the pseudo-rigid-body model, careful decision of the positions of equivalent springs and the values of their spring constants should be made. Here, we use a ninth-order polynomial to model the nonlinear spring stiffness of the mechanism as

$$k = \sum_{i=0}^{9} k_i x^i \tag{7}$$

This ninth-order stiffness function allows for the detailed modeling of the highly nonlinear f-d relation of the mechanism. Third, fifth, seventh, eighth and ninth-order functions have been used to model the highly nonlinear force-displacement curve. The curves generated by the polynomials with order less than nine do not fit the force-displacement curve well.

2.3 Analysis

The equations of motion defined in Eqs. (3)-(7) can be numerically integrated to predict the dynamic behaviors of the mechanism. In order to obtain the nonlinear spring stiffness of the mechanism, finite element analyses are carried out. Due to symmetry, only a quarter model of the mechanism is considered. Fig. 6 shows a schematic of a quarter model with $L_1 = 300$ μm, $L_0 = 900$ μm, $L_s = 200$ μm, $t_1 = 5$ μm, $t_0 = 40$ μm, $t_s = 15$ μm, and $\theta = 2.25^\circ$. The thickness h of the device is 5 μm. A Cartesian coordinate system is also shown in the figure. The displacement in the y direction at $y = 0$ is constrained to represent the symmetry condition due to the mechanism geometry and the loading conditions. Clamped boundary conditions are applied to the fixed ends of the mechanism. A displacement is applied in the $+x$ direction at $y = 0$. Fig. 7 shows a mesh for the quarter model. A mesh sensitivity analysis is performed to assure convergence of the solutions. In the analyses, the material of the device is assumed to be nickel. For the linear elastic and isotropic model, the Young's modulus E is taken as 207 GPa, and the Poisson's ratio ν_p is taken as 0.31. The commercial finite element program ABAQUS [29] is employed to perform the computations. The material properties of electroplated nickel can differ from that of bulk materials because it is highly dependent upon the composition of the plating bath, current density and temperature. Fritz et al. [30] reported that the Young's modulus of electroplated nickel ranges from 205 GPa for a mean current density of 0.2 A/dm^2 to 165 GPa for 2.0 A/dm^2, respectively. The material properties of bulk nickel are used in the finite element analyses in order to understand the f-d relation of the mechanism in the initial design stage. No attempt is made to adjust the material properties to fit the experimental results in this investigation.

A f-d curve and a potential energy curve based on the finite element model are shown in Figs. 8(a) and (b), respectively. We selected a ninth order function, Eq. (7), to fit the simulation data in Fig. 8(a). The values of the coefficients of Eq. (7) are listed in Table 1. As shown in Fig. 8(a), when the displacement of the shuttle mass increases from 0 (the first stable equilibrium position), the force increases initially, reaches its maximum value, then decreases to 0, where is a unstable equilibrium position. When the displacement increases further, the force decreases, attains its minimum value, then increases again and reaches 0, the second stable equilibrium position. As shown in Fig. 8(b), the two local minimums of the energy curve correspond to the two stable equilibrium positions of the mechanism. The local maximum of the curve corresponds to the unstable equilibrium position of the mechanism. The ninth-order stiffness function of Eq. (7) allows for the detailed modeling of the highly nonlinear f-d relation of the mechanism. For polynomials with order less than nine, the maximum actuation force, unstable and stable equilibrium positions of the mechanism are not close to those based on the finite element analyses. Therefore, simulated amplitudes and frequencies of the currents passed through the hinged beams of the mechanism for dynamical switching can be different according to the polynomials selected.

In order to predict the dynamic behaviors of the mechanism, Park stiffly stable method [31] is used to solve the governing nonlinear differential equations, Eqs. (3)-(7). The nonlinearities due to the post-buckling behavior, geometric nonlinearity and Stoke's type damping introduce numerical instability to the integration of the equations. Park method is a robust algorithm available to achieve stable solutions and frequently used for nonlinear dynamic problems with low- and high-frequency range input of the excitation. Using Park method, Eq. (3) can be rewritten as

$$\overline{m} x_{t+\Delta t} = \overline{F}_{t+\Delta t} \tag{8}$$

where the effective mass $\overline{m}$ and effective force $\overline{F}_{t+\Delta t}$ are given by [31]

$$\overline{m} = \frac{100}{36\Delta t^2} m + \frac{10}{6\Delta t} c + k \tag{9}$$

$$\begin{aligned}\overline{F}_{t+\Delta t} = F_{t+\Delta t} + \frac{15}{6\Delta t} m\dot{x}_t - \frac{1}{\Delta t} m\dot{x}_{t-\Delta t} + \frac{1}{6\Delta t} m\dot{x}_{t-2\Delta t} + \left(\frac{150}{36\Delta t^2} m + \frac{15}{6\Delta t} c\right) x_t \\ - \left(\frac{10}{6\Delta t^2} m + \frac{1}{\Delta t} c\right) x_{t-\Delta t} + \left(\frac{10}{36\Delta t^2} m + \frac{1}{6\Delta t} c\right) x_{t-2\Delta t}\end{aligned} \tag{10}$$

where t is time. However, the Park method is not self-starting and requires special starting procedure [32]. It is observed that the calculation of $x_{t+\Delta t}$ involves x and $\dot{x}$ at t, $t-\Delta t$, and $t-2\Delta t$. The initial displacement and velocity can be taken as the displacement x and velocity $\dot{x}$ at t. Following the procedure presented by Lee et al. [26], the Wilson Theta method [31] is used to obtain the displacement x and velocity $\dot{x}$ at $t-\Delta t$ and $t-2\Delta t$.

The values of L_1, L_0, L_s, t_1, t_0, t_s, d, and h used in the numerical integration are 300, 900, 200, 5, 40, 15, 5, and 5 μm, respectively. The value of θ is set to be 2.25°. Many researchers have used the density of bulk nickel, nearly 8900 kg/m^3, for electroplated nickel [33-35]. Teh et al. [36] used a value of 9040 kg/m^3 for the density of their electroplated Ni cantilever. In this investigation, the value of the density of the beam material ρ, electroformed nickel, is taken as 8908 kg/m^3. The values of the dynamic viscosity μ and kinematic viscosity ν of the environmental fluid, air, at 1 atm and 25 °C are taken to be 1.81034×10^{-5} $Pa\cdot s$ and 1.59528×10^{-5} m^2/s, respectively. These values are interpolated from the viscosity values at different temperatures of air at 1 atm [37]. The magnetic field strength B of the permanent magnet is 0.29 tesla. The mechanism is assumed to be driven by an electromagnetic force with a sinusoidal current applied at different frequencies and amplitudes. Simulations are carried out over a frequency range of 2 kHz to 10 kHz with a supply current range of 60 mA to 90 mA peak-to-peak. Fig. 9 shows the time responses of the mechanism based on the numerical integration of Eqs. (8)-(10). As shown in Fig. 9(a), when a current with frequency $\omega/2\pi = 8.8$ kHz and amplitude $i = 80$ mA peak-to-peak is applied through the contact pads, the mechanism initially oscillates around its FSP, and switches to its SSP within $t = 0.5$ msec. Fig. 9(b) shows that when a current with frequency $\omega/2\pi = 9.02$ kHz and amplitude $i = 80$ mA peak-to-peak is applied, the mechanism is found to switch from its SSP to its FSP within $t = 1$ msec.

3. Fabrication and testing

3.1 Fabrication

In order to prove the design of the bistable mechanism for dynamical switching, prototypes of the mechanisms are fabricated. The device has been fabricated by a simple electroforming process on glass substrates. Fig. 10 shows the fabrication steps, where only two masks are used. First, a Cr/Au metallization layer is deposited on the whole glass substrate. Next, a 5 μm-thick photoresist (JSR THB-120N) is coated and patterned to prepare a mold for electrodeposition of a copper sacrificial layer. Then, the photoresist is stripped and a 5 μm-thick photoresist (AZ4620) is coated and patterned on top of the copper sacrificial layer. Into this mold, a 5 μm-thick nickel layer is electrodeposited using a low-stress nickel sulfamate bath with the chemical compositions listed in Table 2. Following that, the photoresist and copper sacrificial layers are removed to release the nickel microstructures. Finally, the Cr/Au layer outside the anchor regions is wet etched for electrical isolation of the electromagnetic actuation. Figs. 11 and 12 show an optical microscope (OM) photo of an array of the fabricated mechanisms, and a close-up view of one mechanism, respectively. Each mechanism in the array is designed for a different driving frequency of the applied current.

3.2 Testing

The fabricated mechanisms are tested using the experimental apparatus shown schematically in Fig. 13, where a permanent magnet of NdFeB (ND-36, Magtech Magnetic Products Co., Taiwan) is attached at the bottom of the glass substrate containing the device array. The substrate and the magnet are held in an acrylic fixture.

The magnet generates a magnetic field strength $B = 0.29$ tesla on the glass substrate in the out-of-plane direction of the substrate. With an AC current passes through the mechanism, an in-plane force is induced to drive the mechanism into vibration. The input sinusoidal AC current is supplied by a function generator (WW5062, Tabor Electronics Ltd., Israel). Experiments are carried out over a frequency range of 2 kHz to 10 kHz with a supply current range of 60 mA to 100 mA peak-to-peak. Fig. 14 is a photo of the experimental apparatus placed under a microscope.

4. Results and discussions

Using the experimental setup, the dynamical switching of the mechanism is successfully realized by the electromagnetic actuation. Figs. 15 and 16 show sequences of snapshots from experiments in atmospheric pressure for forward and backward motions, respectively. A sinusoidal current of 96 mA peak-to-peak with no dc offset is passed through the contact pads at frequency $\omega/2\pi = 2.3$ kHz to dynamically switch the mechanism forward, see Fig. 15. In order to dynamically switch the mechanism backward, a sinusoidal current of 72 mA peak-to-peak with no dc offset is passed through the contact pads at frequency $\omega/2\pi = 3.3$ kHz, see Fig. 16. Based on the measurement from the video images, the maximum displacements of the shuttle mass are nearly 90 μm for both forward and backward motion. They are marked in Figs. 15(e) and 16(a) for forward and backward motion, respectively. The snapshots of the forward and backward motions are taken using a high-speed camera (SpeedCam MiniVis e2, Weinberger, Germany).

The experimental frequencies of the input AC currents for dynamic switching are not close to those based on the simulations. The discrepancy between the experimental and simulated frequencies might come from uncertainties in material properties, geometry and loading conditions used in the simulations. Geometry uncertainty due to fabrication process and Joule heating effects can not be appropriately modeled in simulations. The resonance frequency of the test device measured by a MEMS motion analyzer (MMA G2, Umech Technologies, USA) is 5.1 kHz, which is much lower than that, 7.9 kHz, predicted by the finite element model based on the design parameters. Lee et al. [26] pointed out that the decrease of spring stiffness of a beam structure caused by Joule heating may reduce the resonance frequency. Based on OM observations, the fabricated device is bent upward slightly. A residual tensile stress might have been induced in the beam structure during the fabrication. The residual tensile stress in the beam structure can cause the resonance frequency to increase. It is also revealed by OM inspections that the width measured on the top surface of the beam is less than that of the design and the cross section of the beam is trapezoidal. Due to the non-square cross section of the beam structure, the stiffness of the device is decreased and that might also cause the experimental resonance frequency to be different from the design value.

It is known that Young's modulus of electroplated nickel can be much smaller than that of bulk nickel. Fritz et al. [30] reported Young's modulus of electroplated nickel ranging from 165 GPa for a current density of 20 $\mathrm{A/dm^2}$ during electroplating to 205 GPa for a current density of 0.2 $\mathrm{A/dm^2}$. The current density used in the electroforming process in this investigation is 0.113 $\mathrm{A/dm^2}$. Therefore, the Young's modulus of bulk nickel of 207 GPa is used in the simulations. In order to understand the effects of the Young's modulus on the simulated switching frequency, a f-d relation of the mechanism with a Young's modulus of 177 GPa is obtained by finite element analyses. Using the f-d relation and the numerical integration scheme, the mechanism switches from its FSP to SSP when a current with frequency $\omega / 2\pi = 7.2$ kHz and amplitude $i = 80$ mA peak-to-peak is applied. When a current with frequency $\omega / 2\pi = 8.9$ kHz and amplitude $i = 80$ mA peak-to-peak is applied, the mechanism is found to switch from its SSP to its FSP. These simulated switching frequencies are lower than those based on a higher Young's modulus, 207 GPa, for the electroplated nickel.

As described above, due to the uncertainties in material properties, geometry and loading conditions of the experiments, the frequencies and amplitudes obtained from the simulations for dynamic switching are used only as the guidelines to find the switching frequencies and amplitudes in the experiments.

In order to evaluate the efficiency of the dynamical switching strategy, experiments of statically switching the mechanism is also carried out. For static testing, DC currents are passed through the contact pads using the function generator. The minimum currents needed for static switching of the mechanism forward and backward are found to be 169 and 131 mA, respectively, which are larger than those for dynamical switching, 96 and 72 mA peak-to-peak, respectively.

In the present experimental setup, the volume of the permanent magnet is much larger than the fabricated single device. The sheer volume of the magnet will impose a challenge in the engineering applications of the device. Future work will be the incorporation of a uniform and reliable magnetic field applied by a microcoil to the fabricated devices.

5. Conclusions

A new method to switch a BM by electromagnetic actuation is presented. An electric current passing through the BM placed on top of a permanent magnet creates an electromagnetic Lorenz force. Vibration is utilized to drive the BM on a substrate between its stable positions. The frequencies and amplitudes of the supply current for the dynamic switching are found by solving the nonlinear equation of motion of the BM. The feasibility of using vibration to achieve dynamical switching is confirmed by the derived analytical model. In order to confirm the effectiveness of this approach, prototypes of the device are fabricated on glass substrates using a simple electroforming process. Dynamical switching of the BM at the current of 96 mA and 72 mA peak-to-peak for forward and backward motion, respectively, has been demonstrated. Whereas when the BM is driving statically, higher currents of 169 mA and 131 mA for forward and backward motion, respectively, are needed for switching. The presented switching method provides a simple and efficient means of activating a BM without on-substrate driving mechanisms such as electrostatic or electrothermal actuators.

Acknowledgement

The computing facilities provided by the National Center for High-Performance Computing (NCHC) are greatly appreciated. The measurement equipments provided by National Chip Implementation Center (CIC) and Micro Device Laboratory in NTHU, R.O.C., are greatly appreciated. The authors are also thankful for the financial support from the National Science Council, R.O.C., under Grant No. NSC 96-2221-E-005-095.

References

[1] B.J. Hansen, C.J. Carron, B.D. Jensen, A.R. Hawkins, S.M. Schultz, Plastic latching accelerometer based on bistable compliant mechanisms, Smart Mater. Struct. 16 (2007) 1967-1972.

[2] B. Hälg, On a nonvolatile memory cell based on Micro-Electro-Mechanics, in: Proc. IEEE MEMS 1990 Conference, pp. 172-176.

[3] M. Freudenreich, U. Mescheder, G. Somogyi, Design considerations and realization of a novel micromechanical bi-stable switch, in: Transducers 2003 Workshop, pp. 1096-1099.

[4] N.D. Masters, L.L. Howell, A self-retracting fully compliant bistable micromechanism, Journal of Microelectromechanical Systems 12 (2003) 273-280.

[5] C. Lee, C.-Y. Wu, Study of electrothermal V-beam actuators and latched mechanism for optical switch, J. Micromech. Microeng. 15 (2005) 11-19.

[6] R. Receveur, C.R. Marxer, R. Woering, V. Larik, and N.-F. de Rooij, Lateral moving bistable MEMS DC switch for biomedical applications, Journal of Microelectromechanical Systems 14 (2005) 1089-1098.

[7] E. Kruglick, K. Pister, Bistable MEMS relays and contact characterization**,** in Proc. Solid-state Sensors and Actuators Workshop Cleveland, OH, 1998, pp. 333-337.

[8] T. Gomm, L.L. Howell, R.H. Selfridge, In-plane linear displacement bistable microrelay, J. Micromech. Microeng. 12 (2005) 257-264.

[9] J. Qiu, J.H. Lang, A.H. Slocum, A bulk-micromachined bistable relay with U-shaped thermal actuators, Journal of Microelectromechanical Systems 14 (2005) 1099-1109.

[10] B. Wagner, H.J. Quenzer, S. Hoerschelmann, T. Lisec, M. Juerss, Bistable microvalve with pneumatically coupled membranes, in: Proc. IEEE MEMS 1996 Conference, pp. 384-388.

[11] J. Tsay, L.-Q. Su, C.-K. Sung, Design of a linear micro-feeding system featuring bistable mechanisms, J. Micromech. Microeng. 15 (2005) 63-70.

[12] D.L.Wilcox, L.L. Howell, Fully compliant tensural bistable micromechanisms, Journal of Microelectromechanical Systems 14 (2005) 1223-1235.

[13] J. Casals-Terre, A. Shkel, Snap-action bistable micromechanism actuated by nonlinear resonance, in: IEEE Sensors 2005, pp. 893-896.

[14] Y.-Y. Yang, B.-T. Liao, W.-C. Kuo, A novel 2 X 2 MEMS optical switch using the split cross-bar design, J. Micromech. Microeng. 17 (2007) 875-882.

[15] I.-H. Hwang, Y.-S. Shim, J.-H. Lee, Modeling and experimental characterization of the chevron-type bistable microactuator, J. Micromech. Microeng. 13 (2003) 948-954.

[16] M. Freudenreich, U. Mescheder, G. Somogyi, Simulation and realization of a novel micromechanical bi-stable switch, Sensors and Actuators A 114 (2004) 451-459.

[17] J. Casals-Terre, A. Shkel, Dynamic analysis of a snap-action micromechanism, in: IEEE Sensors 2004, pp. 1245-1248.

[18] H.N. Kwon, I.-H. Hwang, J.-H. Lee, A pulse-operating electrostatic microactuator for bi-stable latching, J. Micromech. Microeng. 15 (2005) 1511-1516.

[19] S. Krylov, B.R. Ilic, D. Schreiber, S. Seretensky, H. Craighead, The pull-in behavior of electrostatically actuated bistable microstructures, J. Micromech. Microeng. 18 (2008) 055026.

[20] J.S. Ko, M.G. Lee, J.S. Han, J. S. Go, B. Shin, D.-S. Lee, A laterally-driven bistable electromagnetic microrelay, ETRI Journal 28 (2006) 389-392.

[21] A. Cao, J. Kim, L. Lin, Bi-directional electrothermal electromagnetic actuators, J. Micromech. Microeng. 17 (2007) 975-982.

[22] M. Sulfridge, T. Saif, N. Miller, K. O'Hara, Optical actuation of a bistable MEMS, Journal of Microelectromechanical Systems 11 (2002) 574-583.

[23] G. Giannopoulos, J. Monreal, J. Vantomme, Snap-through buckling behavior of piezoelectric bimorph beams: II. Experimental verification, Smart Mater. Struct. 16 (2007) 1158-1163.

[24] W. Kreider, A.H. Nayfeh, Experimental investigation of single-mode responses in a fixed-fixed buckled beam, Nonlinear Dynamics 15 (1998) 155-177.

[25] W. Ye, X. Wang, W. Hemmert, D. Freeman, J. White, Air damping in laterally oscillating microresonators: a numerical and experimental study, Journal of Microelectromechanical Systems 12 (2003) 557-566.

[26] K.B. Lee, A.P. Pisano, L. Lin, Nonlinear behaviors of a comb drive actuator under electrically induced tensile and compressive stresses, J. Micromech. Microeng. 17 (2007) 557-566.

[27] J. Qiu, J.H. Lang, A.H. Slocum, A curved-beam bistable mechanism, Journal of Microelectromechanical Systems 13 (2004) 137-146.

[28] L.L. Howell, Compliant Mechanisms, John Wiley & Sons, New York, 2002.

[29] H.D. Hibbitt, B.I. Karlsson, E.P. Sorensen, ABAQUS User Manual, Version 6-2, Providence, RI, USA, 2001.

[30] T. Fritz, M. Griepentrog, W. Mokwa, U. Schnakenberg, Determination of Young's

modulus of electroplated nickel, Electrochimica Acta 48 (2003) 3029-3035.

[31] A.F. D'Souza, V.K. Garg, Advanced Dynamics: Modeling and Analysis, Prentice-Hall, 1984.

[32] T.C. Fung, Complex-time-step Newmark methods with controllable numerical dissipation, International Journal for Numerical Methods in Engineering 41 (1998) 65-93.

[33] M.C. Geear, E.M. Yeatman, A.S. Holmes, R.R.A. Syms, A.P. Finlay, Microengineered electrically resettable circuit breaker, Journal of Microelectromechanical Systems 13 (2004) 887-894.

[34] B. Li, Q. Chen, Design and fabrication of *in situ* UV-LIGA assembled robust nickel micro check valves for compact hydraulic actuators, J. Micromech. Microeng. 15 (2005) 1864-1871.

[35] W.-L. Huang, Z. Ren, C.T.-C. Nguyen, Nickel vibrating micromechanical disk resonator with solid dielectric capacitive-transducer gap, in: Proc. IEEE International Frequency Control Symposium and Exposition 2006, pp. 839-847.

[36] W.H. Teh, R. Crook, C.G. Smith, H.E. Beere, D.A. Ritchie, Characteristics of a micromachined floating-gat high-electron-mobility transistor at 4.2 K, Journal of Applied Physics 97 (2005) 114507.

[37] F.M. White, Fluid mechanics, second edition, McGraw-Hill, Inc., New York, USA, 1986.

Biographies

Dung-An Wang received the Ph.D. degree in mechanical engineering from the University of Michigan at Ann Arbor, in 2004. He is currently an Assistant Professor in the Institute of Precision Engineering, National Chung Hsing University, Taiwan, ROC. His research interests include micromachined resonators and actuators, piezoelectric actuators, microassembly and compliant mechanisms.

Huy-Tuan Pham received the B.S. degree in mechanical engineering from the Ho Chi Minh City University of Technique, Vietnam, in 2005, and the M.S degree from the Institute of Precision Engineering, National Chung Hsing University, Taiwan, ROC., in 2008. He is currently working towards the Ph.D. degree in the Institute of Precision Engineering, National Chung Hsing University, Taiwan, ROC. His research interests are micromachined resonators and actuators, and compliant mechanisms.

Yi-Han Hsieh received the B.S. degree in mechanical engineering from the Southern Taiwan University of Technology, Taiwan, ROC, in 2005, and the M.S degree from the Institute of Precision Engineering, National Chung Hsing University, Taiwan, ROC., in 2008. He is currently an engineer with Taiwan Semiconductor Manufacturing Company Ltd., Taiwan, ROC. His research interests are micromachined resonators and actuators, and compliant mechanisms.

List of figures

Table 1 Values of the coefficients of the nonlinear spring stiffness function.

k_0	2.055×10^{-14}
k_1	-1.412×10^{-11}
k_2	4.132×10^{-9}
k_3	-6.702×10^{-7}
k_4	6.596×10^{-5}
k_5	-4.054×10^{-3}
k_6	1.541×10^{-1}
k_7	-3.427
k_8	35.64
k_9	-7.811

Table 2 Chemical composition and operation conditions for the low-stress nickel electroplating solution.

Chemical/Plating Parameter	Amount/Value
Nickel sulfamate ($Ni(NH_2SO_3)_2\cdot4H_2O$)	450 g/L
Boric acid (H_3BO_3)	35 g/L
Nickel chloride ($NiCl_2\cdot6H_2O$)	4 g /L
Stress reducer	17 ml/L
Leveling agent	17 ml/L
Wetting agent	2 ml/L
Bath temperature	45 °C
Plating current type	dc current
pH of the solution	4
Plating current density	0.113 A/dm^2
Deposition rate	0.071 μm/min
Anode-cathode spacing	100 mm
Anode type	titanium

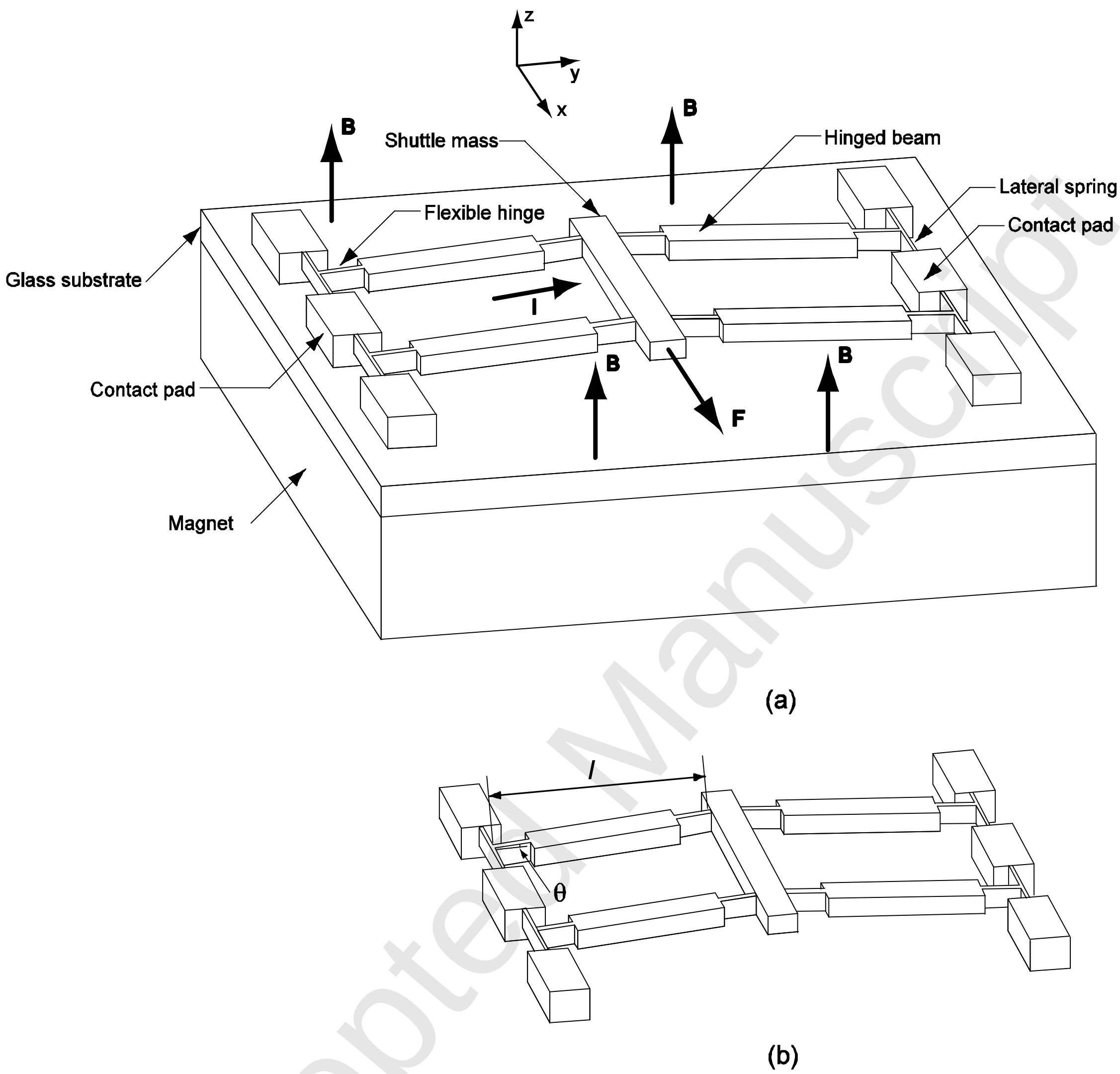

Fig. 1 (a) A schematic of a BM and a permanent magnet served to actuate the mechanism. (b) Length l and the angle θ with respect to the y axis.

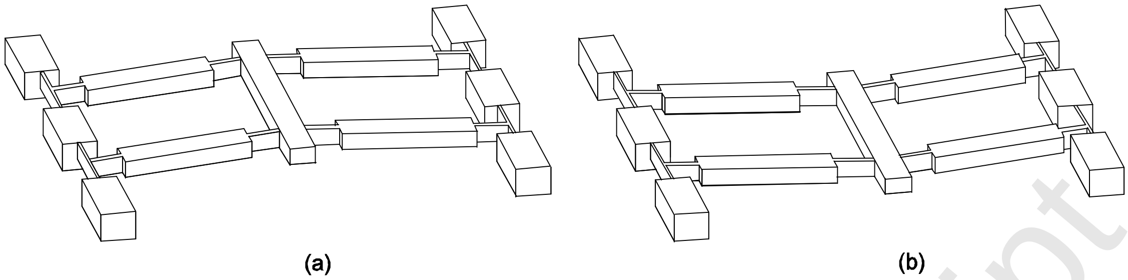

Fig. 2 Two stable equilibrium states of the mechanism.

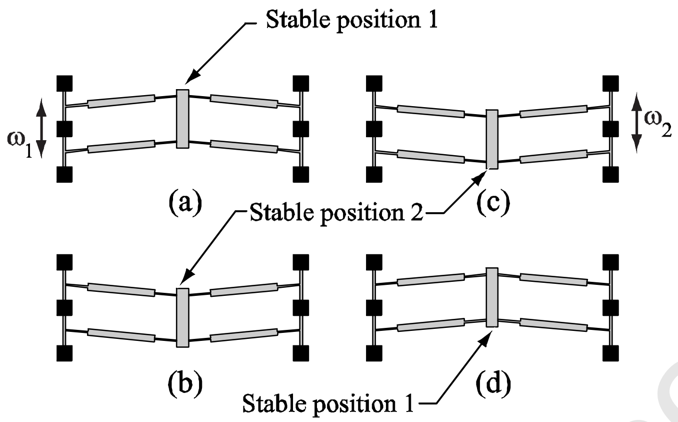

Fig. 3 Four-step operation of the mechanism.

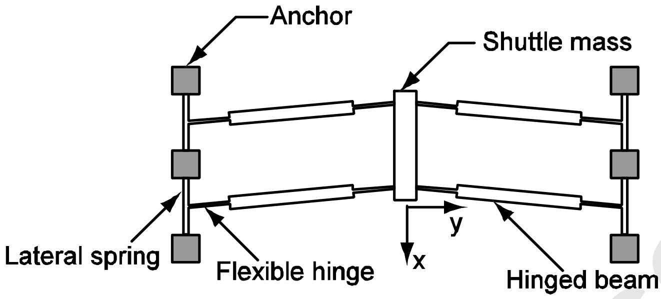

Fig. 4 A schematic of a BM.

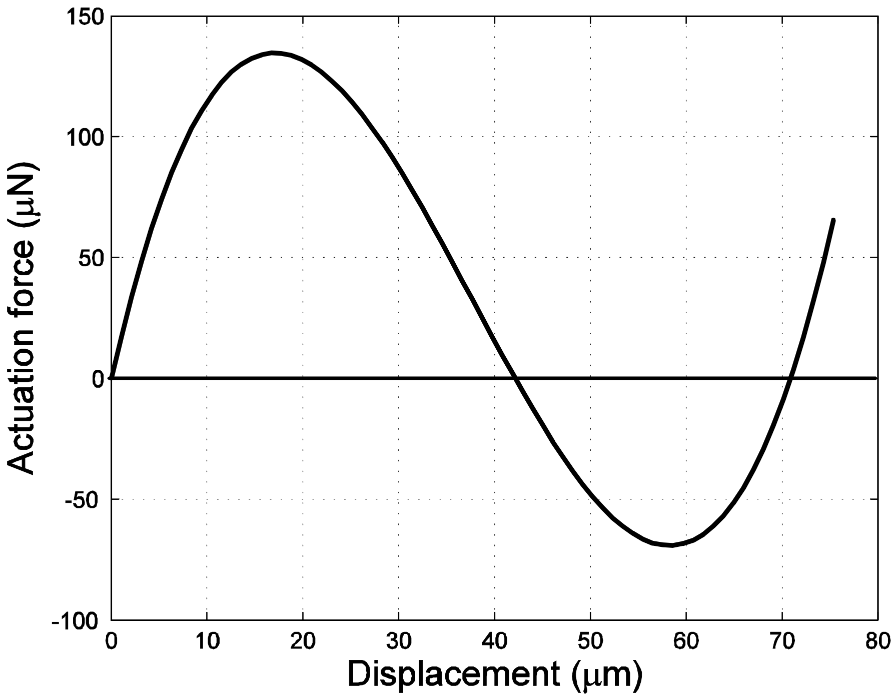

Fig. 5 A typical f-d curve of a BM.

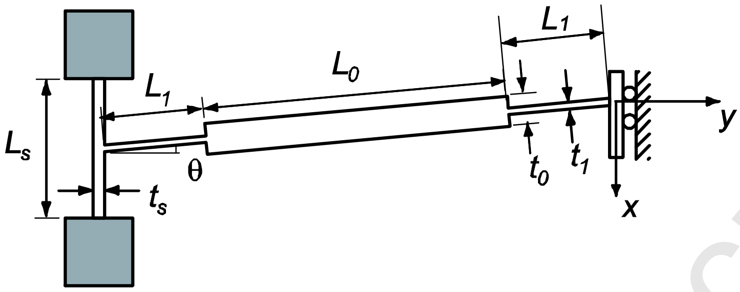

Fig. 6 A schematic of a quarter model.

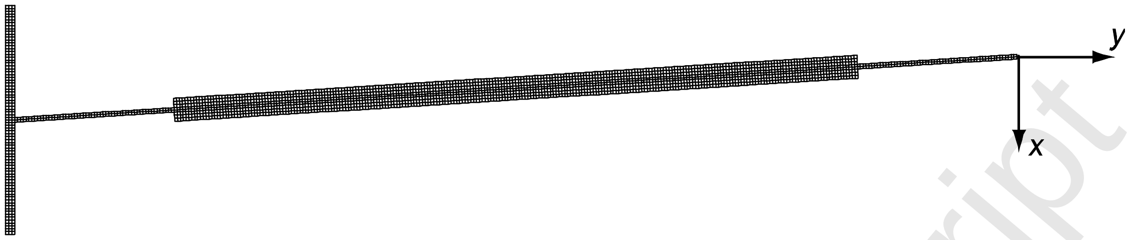

Fig. 7 A mesh for the quarter model.

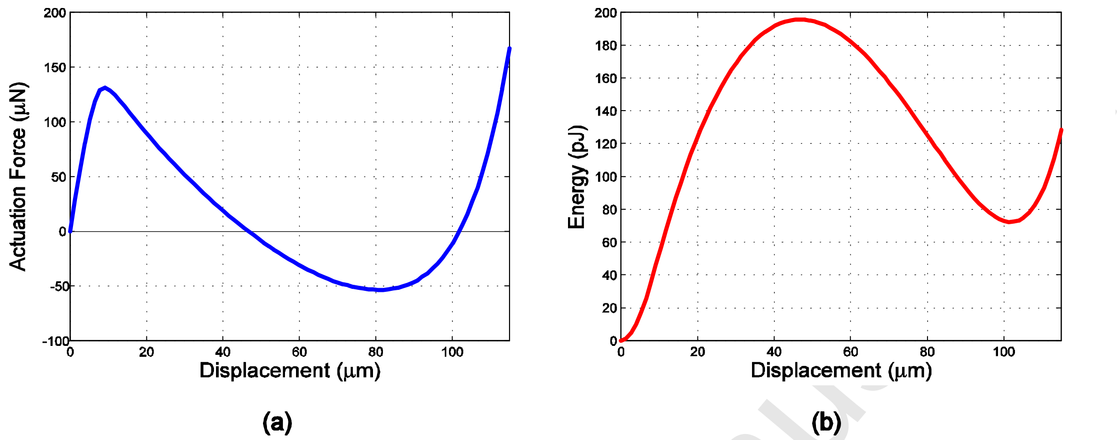

New figure

Fig. 8 F-d curve and potential energy curve based on the finite element model.

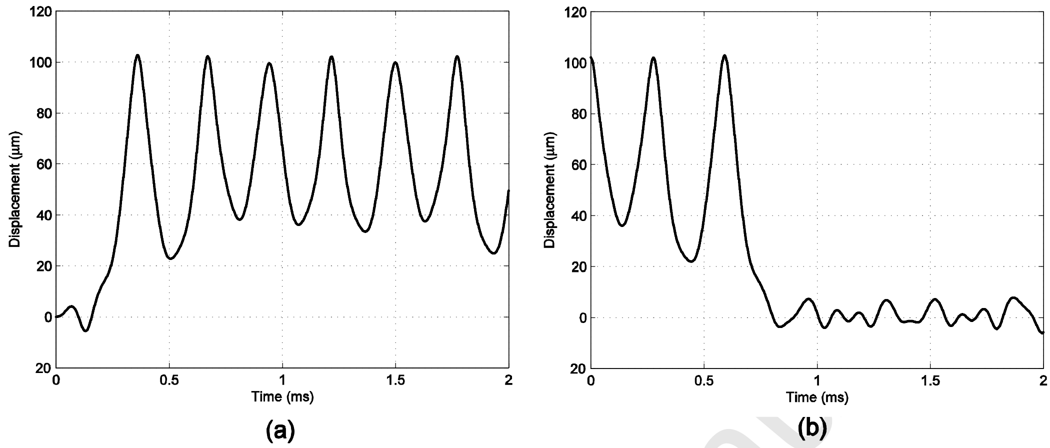

Fig. 9 Time responses of the mechanism. (a) Switching from FSP to SSP; (b) switching from SSP to FSP.

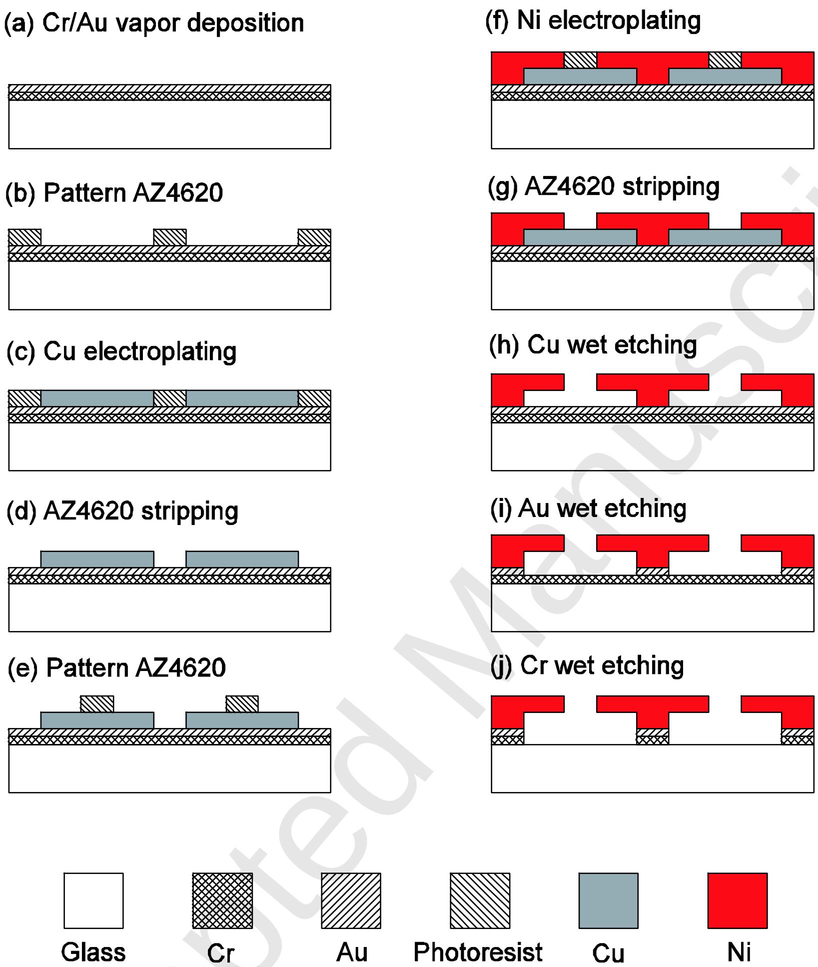

Fig. 10 Fabrication steps.

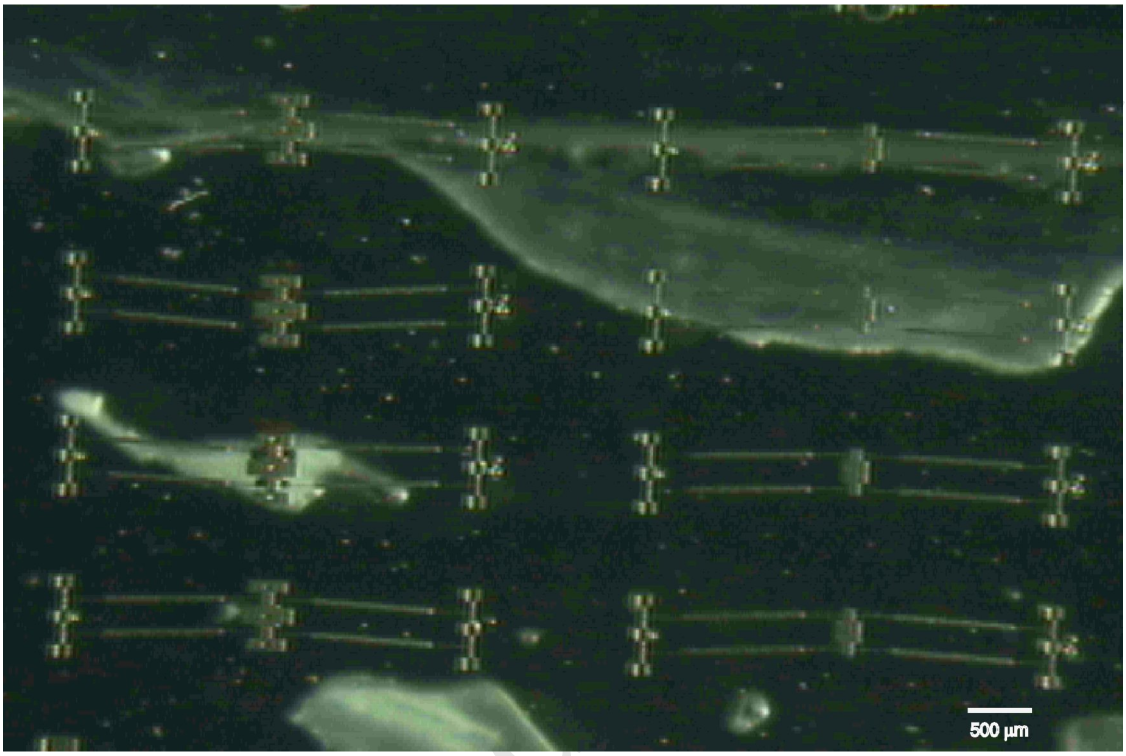

Fig. 11 An array of fabricated devices.

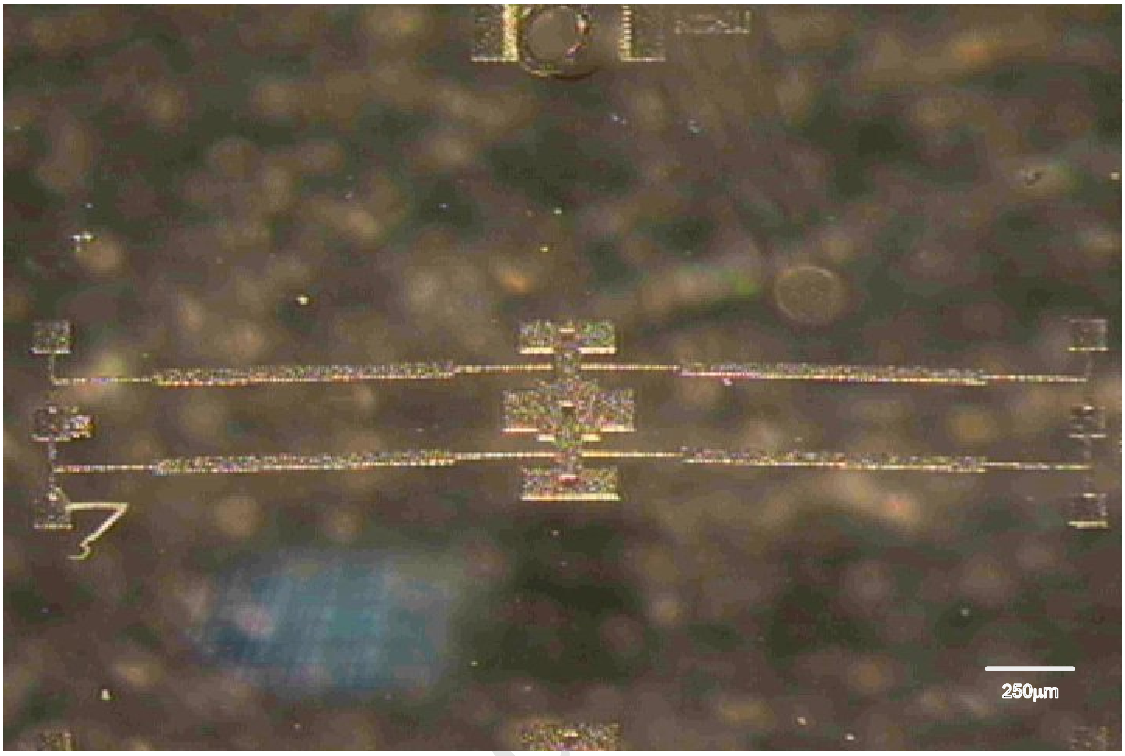

Fig. 12 An OM photo of a fabricated device.

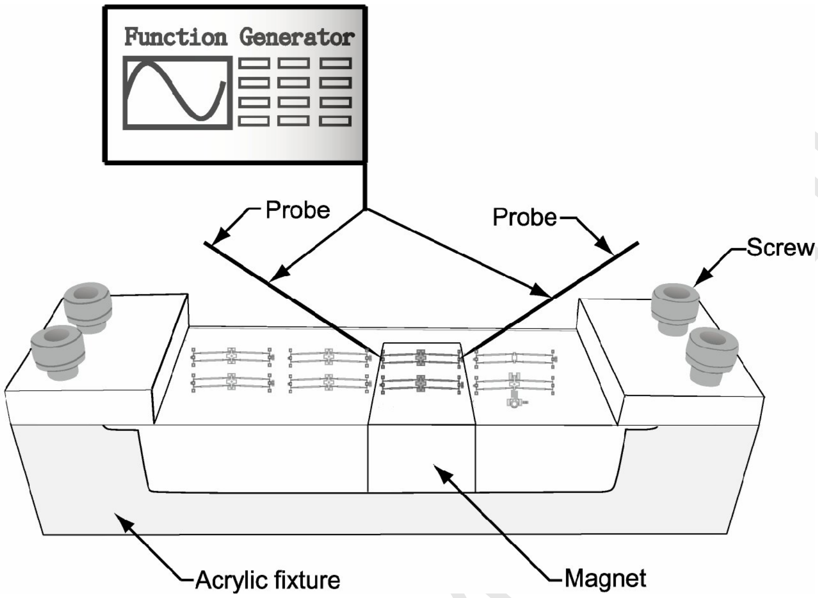

Fig. 13 A schematic of the experimental setup.

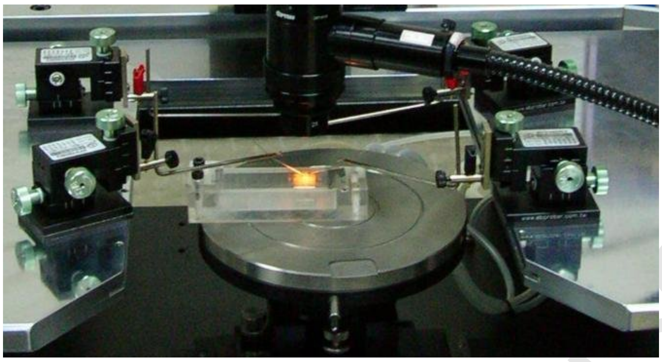

Fig. 14 Experimental apparatus placed under a high-speed camera.

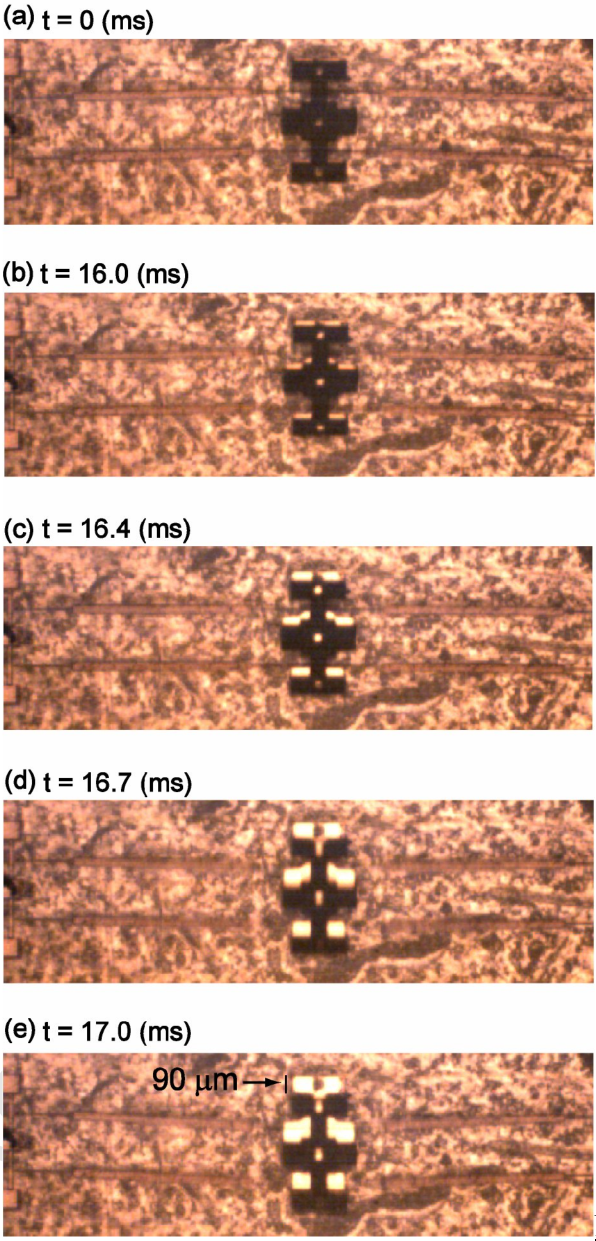

New figure

Fig. 15 Snapshots for forward motion.

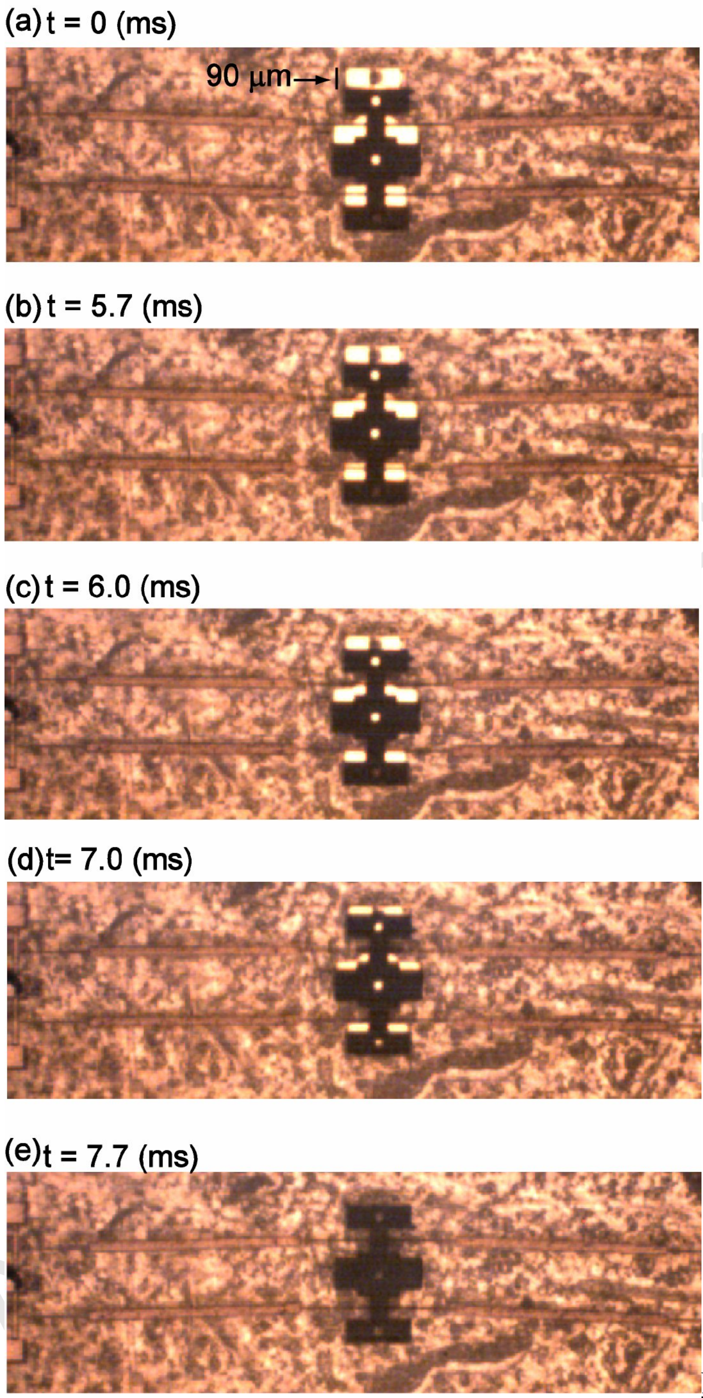

New figure

Fig. 16 Snapshots for backward motion.